

Unravelling the sources of carbon emissions at the onset of Oceanic Anoxic Event (OAE) 1a

Adloff, Markus; Greene, Sarah; Parkinson, Ian J.; Naafs, B. David A.; Preston, Will; Ridgwell, Andy; Lunt, Dan J.; Castro Jiminez, Jose Manuel; Monteiro, Fanny M.

DOI:

[10.1016/j.epsl.2019.115947](https://doi.org/10.1016/j.epsl.2019.115947)

License:

Creative Commons: Attribution-NonCommercial-NoDerivs (CC BY-NC-ND)

Document Version

Peer reviewed version

Citation for published version (Harvard):

Adloff, M, Greene, S, Parkinson, IJ, Naafs, BDA, Preston, W, Ridgwell, A, Lunt, DJ, Castro Jiminez, JM & Monteiro, FM 2020, 'Unravelling the sources of carbon emissions at the onset of Oceanic Anoxic Event (OAE) 1a', *Earth and Planetary Science Letters*, vol. 530, 115947. <https://doi.org/10.1016/j.epsl.2019.115947>

[Link to publication on Research at Birmingham portal](#)

General rights

Unless a licence is specified above, all rights (including copyright and moral rights) in this document are retained by the authors and/or the copyright holders. The express permission of the copyright holder must be obtained for any use of this material other than for purposes permitted by law.

- Users may freely distribute the URL that is used to identify this publication.
- Users may download and/or print one copy of the publication from the University of Birmingham research portal for the purpose of private study or non-commercial research.
- User may use extracts from the document in line with the concept of 'fair dealing' under the Copyright, Designs and Patents Act 1988 (?)
- Users may not further distribute the material nor use it for the purposes of commercial gain.

Where a licence is displayed above, please note the terms and conditions of the licence govern your use of this document.

When citing, please reference the published version.

Take down policy

While the University of Birmingham exercises care and attention in making items available there are rare occasions when an item has been uploaded in error or has been deemed to be commercially or otherwise sensitive.

If you believe that this is the case for this document, please contact UBIRA@lists.bham.ac.uk providing details and we will remove access to the work immediately and investigate.

Unravelling the sources of carbon emissions at the onset of Oceanic Anoxic Event (OAE) 1a

Markus Adloff^{a,*}, Sarah E. Greene^b, Ian J. Parkinson^c, B. David A. Naafs^{d,c},
Will Preston^c, Andy Ridgwell^{e,a}, Dan J. Lunt^a, José Manuel Castro Jiménez^f,
Fanny M. Monteiro^a

^a*School of Geographical Sciences, University of Bristol, University Road, BS81SS, UK*

^b*School of Geography, Earth and Environmental Sciences, University of Birmingham, Edgbaston, B152TT, UK*

^c*School of Earth Sciences, University of Bristol, Queen's Road, BS81RJ, UK*

^d*School of Chemistry, University of Bristol, Cantock's Close, BS81TS, UK*

^e*Department of Earth Sciences, University of California Riverside, 900 University Ave, Riverside, CA 92521, USA*

^f*Departamento de Geología, CEACTION, Universidad de Jaén, Campus Las Lagunillas s/n, 23071 Jaén, Spain*

Abstract

The early Aptian Oceanic Anoxic Event (OAE) 1a represents a major perturbation of the Earth's climate system and in particular the carbon cycle, as evidenced by widespread preservation of organic matter in marine settings and a characteristic negative carbon isotopic excursion (CIE) at its onset, followed by a broad positive CIE. The contemporaneous emplacement of a large igneous province (LIP) is invoked as a trigger for OAE 1a (and OAEs in general), but this link and the ultimate source of the carbon perturbation at the onset of OAEs is still debated. In this study, we simultaneously assimilate an atmospheric $p\text{CO}_2$ reconstruction along with a $\delta^{13}\text{C}$ record from the Spanish Cau section in an Earth system model to obtain a novel transient reconstruction of emission rates and identify the primary carbon-emitting sources across the negative CIE interval at the onset of OAE 1a. We reconstruct carbon emissions of 4,300 -

*Corresponding author

Email address: markus.adloff@bristol.ac.uk (Markus Adloff)
Preprint submitted to *Earth and Planetary Science Letters*

November 7, 2019

28 29,200 Pg from a mixture of carbon sources. This estimate is a lower bound,
29 as contemporaneous organic carbon burial is not accounted for. Carbon was
30 first released at slow rates from a ^{13}C -depleted reservoir (e.g. thermo- and/or
31 biogenic methane from sill intrusions). Towards the end of the negative CIE
32 the rate of emissions increased and they became more ^{13}C -enriched, likely from
33 a dominantly volcanic source (e.g. LIPs). New osmium isotope ($^{187}\text{Os}/^{188}\text{Os}$)
34 measurements, from the same section as the $p\text{CO}_2$ reconstruction and $\delta^{13}\text{C}$
35 data, reveal a shift to less radiogenic values coinciding with the change towards
36 mantle-derived carbon emissions as indicated by our modelling results, lending
37 further support to our interpretation. These results highlight that geologically
38 triggered carbon emissions were likely driving the OAE onset.
39 *Keywords:* Aptian, data assimilation, carbon source, osmium isotopes,
40 volcanism

41 1. Introduction

42 The early Aptian Oceanic Anoxic Event (OAE) 1a (~ 121 Ma, Olierook et al.,
43 2019) represents one of the largest perturbations of the climate system during
44 the last 200 Myr (Jenkyns, 2010). Although OAEs, including OAE 1a, were first
45 identified in the 1970s (Schlanger & Jenkyns, 1976), it is still unclear exactly how
46 the oceanic system evolved into such an extreme state. Increasing nutrient sup-
47 ply to the photic zone and, to a lesser extent, climate warming may have played
48 a crucial role (Larson & Erba, 1999; Jenkyns, 2010; Monteiro et al., 2012), driv-
49 ing increased productivity and subsurface oxygen demand, and reduced oxygen

50 solubility, respectively. The resulting reduced oceanic oxygen concentrations
51 would have led to enhanced preservation and burial of organic matter (Jenkyns,
52 2010; Monteiro et al., 2012). However, the driver of this warming and increased
53 nutrient delivery is debated.

54 While all OAEs are associated with a positive carbon isotopic excursion
55 (CIE), interpreted as reflecting an interval of enhanced burial of organic matter,
56 the onset of OAE 1a is characterized by a distinct negative CIE prior to the
57 positive CIE (Menegatti et al., 1998). Because of the broad temporal coincidence
58 of OAE 1a with the emplacement of the Ontong-Java Plateau, the negative CIE
59 could have resulted from carbon input from (submarine) volcanism initiating
60 the OAE by warming the climate and releasing nutrients to the ocean (e.g.
61 Weissert, 1989). A phase of increased volcanism during the onset of OAE 1a
62 (and other OAEs) is further highlighted by the observed perturbations of the
63 marine osmium cycle (Tejada et al., 2009; Bottini et al., 2012). However, it is
64 not certain whether volcanic emissions could have caused the negative CIE, so
65 destabilization of methane hydrates has been proposed as an alternative, more
66 ^{13}C -depleted carbon source (Beerling et al., 2002; van Breugel et al., 2007;
67 Méhay et al., 2009; Malinverno et al., 2010).

68 Constraining the carbon source for OAE 1a is crucial as it has implications
69 for the mass and rate of carbon emissions and hence extent of the perturba-
70 tion estimated from the carbon isotope record. The size of a negative CIE
71 is a function of the mass of emitted carbon and its isotopic composition (e.g.
72 Kirtland-Turner & Ridgwell, 2016), a predominantly volcanic carbon source

(CO₂), relatively enriched in ¹³C compared to organic carbon sources, requires massive carbon emissions to match the negative CIE, resulting in high atmospheric CO₂ concentrations (e.g. 3000 ppm *p*CO₂ increase (Bauer et al., 2017)). In contrast, the estimated emissions, and hence CO₂ concentrations, are much lower if the carbon originated predominantly from more ¹³C-depleted sources (e.g. 600 ppm for methane emissions (Beerling et al., 2002)).

The nature of the dominant carbon source is important to determine the role of Earth system feedbacks in triggering OAE formation in the Aptian and its sensitivity to carbon injections. For instance, predominant volcanic CO₂ emissions suggest OAE formation was primarily a response to external forcing while a dominant biogenic methane source would indicate a major role for feedbacks between surface carbon reservoirs and an increased sensitivity to carbon emissions. This could have broader implications for our understanding of the formation of other Mesozoic OAEs since negative CIEs are also known from OAE 1b and the Toarcian OAE, and the presence of a suppressed negative CIE before OAE 2 is discussed (Jenkyns, 2010).

Recently, a continuous *p*CO₂ proxy record across OAE 1a (Naafs et al., 2016) together with a $\delta^{13}\text{C}_{carb}$ record from the same site provides an opportunity to identify the carbon source and quantify emissions rates across OAE 1a. The *p*CO₂ record, based on compound-specific and bulk $\delta^{13}\text{C}_{carb}$ from the hemipelagic Tethyan Cau section, shows a gradual *p*CO₂ increase during the negative CIE starting around 800-1000 ppm and reaching maximum values of 2000 ± 1200 ppm before the recovery of the negative CIE. This estimate is within

96 the range of previously reconstructed $p\text{CO}_2$ values during the Early Cretaceous
 97 of 200-2000 ppm (see Wang et al., 2014, for a compilation) and is between $p\text{CO}_2$
 98 values predicted for a pure methane and a purely volcanic source. At the same
 99 time as the $p\text{CO}_2$ increase, organic proxies indicate a 2-5 °C increase in lo-
 100 cal sea-surface temperature (SST) during the negative CIE (Mutterlose et al.,
 101 2014; Naafs & Pancost, 2016). Global temperature changes of this magnitude
 102 are consistent with a doubling to quadrupling of $p\text{CO}_2$, depending on assump-
 103 tions about the initial $p\text{CO}_2$ and the climate sensitivity of the Early Cretaceous.
 104 At the same time, biological turn-over and carbonate platform drowning, key
 105 features of OAE 1a, have been interpreted as being the results of surface ocean
 106 acidification due to increased $p\text{CO}_2$ (Wissler et al., 2003; Erba et al., 2010).
 107 However, it is debated whether the relative timing, the amount, and the rate of
 108 emitted carbon explain the observed changes (Gibbs et al., 2011; Naafs et al.,
 109 2016).

110 In this study, we assimilate the observed negative CIE and reconstructed
 111 $p\text{CO}_2$ changes from the Cau section in the Earth system model cGENIE (Ridg-
 112 well et al., 2007) to constrain carbon emissions across the onset of OAE 1a and
 113 to understand their implications for the dominant carbon sources. We also as-
 114 sess the effect of the $p\text{CO}_2$ changes on Earth’s climate, as well as quantifying
 115 the implications of uncertainties in $p\text{CO}_2$ change estimates and duration of the
 116 OAE onset for reconstructing the carbon cycle perturbation. Finally, we com-
 117 pare our simulation results to a newly-generated osmium isotope record from
 118 the same section, which allows us to reconsider the relationship between the

negative CIE and environmental perturbations at the onset of OAE 1a.

2. Methods

2.1. The Cau section

The studied succession belongs to the Almadich Formation, made of a cyclic succession of hemipelagic marls and marlstones of late Barremian- Aptian p.p. age (Aguado et al., 1999; Castro et al., 2008). The interval considered in this study is located in the upper part of the lower member of the Almadich Formation, of Early Aptian age (Desayesites forbesi ammonite zone, B. blowi planktonic foraminifera, see Naafs et al., 2016). The lithologies present are dominant grey marls (beds 0.5 – 2.5 m thick) alternating with marly limestones (beds 0.3 – 0.6 m thick), with two levels of dark marls (ca. 0.4 m thick) containing small pyrite nodules. The samples used for Os analyses were taken from the marly limestone levels, that have a CaCO_3 content between 36 and 70% wt and TOC contents ranging from <0.7 to 2.4% wt. We assume stratigraphic continuity and a constant sedimentation rate as there is no sedimentological evidence for interruption of sedimentation (hard/soft-ground or erosive surfaces). Also biostratigraphy and nannofossils associations are consistent with a continuous record, at the scale of the resolution available (Aguado et al., 1999; Naafs et al., 2016).

2.2. Model setup and experiment design

cGENIE is the carbon cycle centric version of the Grid ENabled Integrated Earth system model (GENIE), which couples a 3D ocean with a 2D zonally-

141 averaged atmosphere (Edwards & Marsh, 2005), accounting for the biogeochem-
142 ical cycles of carbon, phosphorus, sulphur, oxygen and stable carbon isotopes
143 (Ridgwell et al., 2007). cGENIE can be run with a vertically-integrated sediment
144 module which builds up deep sea sediments with varying CaCO_3 content and
145 carbon isotopic composition, resolving for CaCO_3 burial and dissolution (Ridg-
146 well & Hargreaves, 2007) and with a terrestrial weathering module (Colbourn
147 et al., 2013) hence closing the geological carbon cycle. Its design also allows for
148 inversion (data assimilation) experiments (e.g. Cui et al., 2011; Gutjahr et al.,
149 2017, see below).

150 Here we ran the model on a 36x36 grid with 16 vertical levels in the ocean,
151 and included modules for weathering and marine sediments by which alkalinity
152 is added to or removed from the ocean.

153 In our model set-up, carbon emissions affect temperature, weathering rates,
154 ocean solubility of gases, and ocean circulation. Wind fields are fixed and pre-
155 scribed as boundary conditions and hence do not change in response to changing
156 atmospheric CO_2 concentration and greenhouse warming.

157 We configured cGENIE for the early Aptian using paleogeography and bathymetry
158 (see Appendix A), wind fields, and planetary albedo from the Aptian modelling
159 setup of Donnadieu et al. (2006). Temperature effects on biogeochemical pro-
160 duction were included, and remineralization profiles adapted to a warmer ocean
161 (John et al., 2014). We spun up the model in a first step (20 kyr) to equilibrate
162 to an atmospheric CO_2 concentration of 840 ppm (as reconstructed for the start
163 of the negative CIE in Naafs et al. (2016)) and atmospheric $\delta^{13}\text{C}$ value of -6

164 ‰, which is at the upper limit of measured values of the modern atmospheric
 165 composition (Craig, 1953). Carbonate production is set up as in Ridgwell &
 166 Schmidt (2010) to represent a warm, ice-free world. We assume that organic
 167 carbon burial did not play a major role for the marine carbon cycle during the
 168 interval that we simulate here (see Discussion section), but in order to equili-
 169 brate oceanic $\delta^{13}\text{C}$ in the absence of organic carbon burial, we set the carbon
 170 isotopic composition of the weathering flux to 6.2 ‰. Initial calcium ion supply
 171 from terrestrial weathering is set to 34 Pmol yr^{-1} , resulting in an average sur-
 172 face calcite saturation state (4.3) within the reconstructed range for the Early
 173 Cretaceous (Ridgwell & Zeebe, 2005). The initial oceanic nutrient inventory
 174 was set to $1.06 \mu\text{mol PO}_4^{3-} \text{ kg}^{-1}$ ocean water, equalling half of the preindus-
 175 trial oceanic phosphate inventory. This is based on a model-data comparison
 176 of pre-OAE 1a anoxia extents, following Monteiro et al. 2012 (see appendix
 177 G). However, sensitivity experiments showed that the initial phosphate inven-
 178 tory has little effect on our results (see fig. D2 in the appendix). During the
 179 second spin up stage (500 kyr), the model was run as an open system so that
 180 volcanic outgassing, riverine input of solutes to the ocean, and carbonate burial
 181 in marine sediments could reach equilibrium.

182 To constrain carbon fluxes and their isotopic composition across OAE 1a
 183 onset, we used a double data assimilation approach. Similar studies with single
 184 assimilations used the size of negative CIEs to constrain emission rates associ-
 185 ated with other major carbon cycle events such as the Paleocene-Eocene Ther-
 186 mal Maximum (PETM, e.g. Cui et al., 2011; Turner & Ridgwell, 2013) making

assumptions about the $\delta^{13}\text{C}$ signature of the carbon source. Here however, we intend to reconstruct both the mass and provenance (i.e. isotopic composition) of the emitted carbon. Knowing that a given isotopic excursion can be produced by adding a small mass of very ^{13}C -depleted carbon or a large mass of less ^{13}C -depleted carbon (e.g. Kirtland-Turner & Ridgwell, 2016) this constitutes a problem with two unknowns (mass and composition), the solution for which requires an additional constraint to the CIE size. We hence combined estimates of atmospheric $\delta^{13}\text{C}$ changes with estimates of $p\text{CO}_2$ changes (Naafs et al., 2016) to reconstruct carbon emissions across the onset of the OAE 1a negative CIE.

Each time step, cGENIE adds the mass of carbon needed to reach the prescribed $p\text{CO}_2$ target to the atmosphere, and then calculates the required isotopic signature of that carbon addition to create the right CIE. We allow a maximum carbon emission rate of 10 Pg yr^{-1} with a $\delta^{13}\text{C}$ not more negative than -100 ‰ . We used the Naafs et al. (2016) $p\text{CO}_2$ estimates based on $\Delta^{13}\text{C}$, the offset between compound specific $\delta^{13}\text{C}$ in organic matter and bulk carbonate $\delta^{13}\text{C}$ ($\delta^{13}\text{C}_{carb}$) (Popp et al., 1998). We assumed that the evolution of $\delta^{13}\text{C}_{carb}$ reflects marine and atmospheric $\delta^{13}\text{C}$ changes (see Appendix C). For this, we correct sedimentary $\delta^{13}\text{C}$ measurements from the Cau section by applying a 7.7 ‰ offset to account for different baseline $\delta^{13}\text{C}$ values between atmosphere and biogenic CaCO_3 . We smooth these data by applying a running mean over 7 data points (see fig. 1) to minimize the effect of short-term fluctuations. This smoothed sedimentary $\delta^{13}\text{C}$ is characterized by an averaged 1.3 ‰ negative

210 excursion (maximum value 1.6 ‰), which is similar to most other measured
 211 negative CIE amplitudes for OAE 1a (see Appendix B). This dual data assim-
 212 ilation exercise is analogous to Gutjahr et al. (2017)’ assessment of the PETM
 213 carbon cycle perturbation, except here taking pelagic $\delta^{13}\text{C}_{carb}$ as a measure of
 214 atmospheric rather than surface ocean (DIC) $\delta^{13}\text{C}$ changes, and we directly
 215 constrain the rate of emissions using a $p\text{CO}_2$ reconstruction rather than surface
 216 pH.

217 We additionally address a number of uncertainties in the data and its in-
 218 terpretation. Firstly, implications of uncertainties in the $p\text{CO}_2$ reconstruction
 219 are explored by using an ensemble of 5 simulations with different $p\text{CO}_2$ tra-
 220 jectories within the uncertainty envelope reconstructed by Naafs et al. (2016)
 221 (fig. 1). This uncertainty envelope accounts for uncertainties in the calibration
 222 of the $p\text{CO}_2$ reconstruction method to Cretaceous organisms and due to the
 223 fluctuability of the ^{13}C curve in Cau outcrop data. Secondly, the duration of
 224 the negative CIE at the OAE 1a onset is poorly constrained. We run every
 225 $p\text{CO}_2$ scenario with a duration of 100 kyr, but since durations between 20 and
 226 300 kyr have been suggested for the onset of the negative CIE interval (e.g. van
 227 Breugel et al., 2007; Li et al., 2008; Malinverno et al., 2010; Hu et al., 2012),
 228 we repeat some simulations with three different assumed durations: 20 kyrs, 40
 229 kyrs and 300 kyrs. In total, we run 20 inverse modelling simulations, exploring 5
 230 different $p\text{CO}_2$ trajectories and 4 different assumptions about durations. Addi-
 231 tional sensitivity experiments were run to investigate the sensitivity to boundary
 232 conditions (see Appendix).

233 2.3. Osmium isotope analysis

234 Osmium (Os) isotopes and Os and Rhenium (Re) concentrations were de-
235 termined at the School of Earth Sciences, University of Bristol. Samples were
236 digested in Carius tubes using techniques slightly modified from Shirey & Walker
237 (1995). 0.3-0.5 g of powder was added to the Carius tubes. As the rock con-
238 tained a significant amount of carbonate (46 m - 62 m of the Cau section consist
239 of a succession of marl and marly limestone, see Quijano et al. (2012) and Naafs
240 et al. (2016) for more information on the lithologies) the powder was decarbon-
241 ated with a small amount of concentrated HCl prior to sealing. Appropriate
242 amounts of ^{190}Os and ^{185}Re spikes were added to the Carius tubes along with
243 additional HCl and HNO_3 to make up 12 ml of inverse aqua regia. The samples
244 were then digested at 230 °C for 48 hours. This technique recovers hydrogenic
245 Os and Re without dissolving any detrital material.

246 Os and Re separation chemistry and mass spectrometry follows methods re-
247 cently described in detail elsewhere (Josso et al., 2019). For Os isotope analyses
248 the purified Os was analysed on a ThermoFisher Triton thermal ionisation mass
249 spectrometer (TIMS) in N-TIMS mode, with instrumental mass fractionation
250 corrected for using the exponential mass fractionation law and a $^{192}\text{Os}/^{188}\text{Os}$
251 ratio of 3.08271. Os concentrations were determined by isotope dilution and the
252 isotope data were spike-stripped to yield the sample $^{187}\text{Os}/^{188}\text{Os}$ ratio. Total
253 procedural blanks were determined for each dissolution batch and yielded Os
254 concentrations of 0.31 and 1.46 pg, with $^{187}\text{Os}/^{188}\text{Os}$ ratios of 0.1783 ± 0.0347
255 and 0.1745 ± 0.0557 respectively. All data were corrected for the procedural

256 blank with blank corrections usually less than 1.5 % (range 0.04 to 4 %) on the
 257 concentration and usually less than 1 % (range 0.02-3.5 %) on the $^{187}\text{Os}/^{188}\text{Os}$
 258 ratio depending on sample size and Os concentration. A DTM solution standard
 259 was run during the analytical period and yielded a $^{187}\text{Os}/^{188}\text{Os}$ ratio of 0.17396
 260 ± 39 (2sd, n=12), within error of previous determinations of the standard (e.g.
 261 Birck et al., 1997). Precision on the standard and samples is similar because
 262 they were both run at comparable beam intensity, with the exception of one
 263 sample, which has a precision of 12 ‰.

264 Re isotopes were measured by multi-collector inductively plasma source mass
 265 spectrometry (MC-ICP-MS) on a ThermoFisher Neptune using a SEM and
 266 corrected for instrumental mass fractionation using the exponential mass frac-
 267 tionation law and a $^{191}\text{Ir}/^{193}\text{Ir}$ ratio of 0.59418. Total procedural blanks were
 268 determined for each dissolution batch and yielded Re concentrations of 5 ± 2
 269 pg, with Re concentrations determined by isotope dilution and blank corrected
 270 using the appropriate procedural blank. Blank corrections for the Re concen-
 271 trations are less than 2 % (range 0.14-4.1 %). A 9 ppt solution of the NIST
 272 SRM3134 Re standard, doped with Ir, was run during the analytical period and
 273 yielded a $^{187}\text{Re}/^{185}\text{Re}$ ratio within error of previous determinations of the stan-
 274 dard (Miller et al., 2009). One sample (Cau-21) was fully duplicated, because
 275 it had elevated Re concentrations, low Os concentrations and gave a low initial
 276 $^{187}\text{Os}/^{188}\text{Os}$ ratio at a key part of the section. The duplicate analyses gave
 277 initial $^{187}\text{Os}/^{188}\text{Os}$ ratios just outside of analytical uncertainty, but confirming
 278 that there is significant drop in initial $^{187}\text{Os}/^{188}\text{Os}$ ratio in the section at this

time.

3. Results

The model simulations provide estimates of carbon emission rates and the isotopic composition of the emitted carbon for the onset of the Aptian negative CIE under different $p\text{CO}_2$ change scenarios (fig. 2a-b) and onset durations (fig. 2c-d). In our simulations, total emissions ranged between 4,300-29,200 Pg C with emission rates between 0.01 and 0.7 Pg C yr^{-1} . The uncertainty in our carbon emission estimates is almost equally attributable to uncertainties in the duration of the event and the $p\text{CO}_2$ reconstruction (10,300 Pg C and 13,700 Pg C respectively). Alternative assumptions on initial atmospheric CO_2 concentrations, oceanic nutrient inventory and surface ocean saturation state add only minor additional uncertainty to emission rates (see sensitivity studies in Appendix D). The model results imply isotopically light carbon input (mean composition across all scenarios = -42 ‰) at the start of the negative CIE (46 - 50 m) for all scenarios. Toward the peak of the negative CIE, our model results indicate a shift towards the input of less ^{13}C -depleted carbon with a mean composition of -6 ‰ between 55.5 - 60.0 m. Additional sensitivity studies (see Appendix D) demonstrate that the necessity for ^{13}C -depleted carbon at the start of the negative CIE is a robust result considering uncertainties in initial atmospheric CO_2 concentration, initial oceanic nutrient inventory, initial carbonate saturation state, and different biological production schemes (temperature-dependent or -independent production).

301 In our simulations the calcite saturation state (Ω) of the surface ocean only
 302 decreases appreciably in experiments with carbon emission rates of at least
 303 0.1 Pg C yr^{-1} (see fig. F1 in Appendix F). In scenarios with slower carbon
 304 emissions, surface ocean Ω stays constant or increases slightly. The total Ω
 305 change and the associated uncertainty intervals vary between locations and are
 306 largest in the tropics (up to ~ -2.5 in the most extreme experiments, see fig.
 307 F2 in Appendix F). Sea surface temperature (SST) changes are more variable
 308 with $p\text{CO}_2$ change scenario than assumed CIE onset duration, and are largest
 309 around Antarctica (see fig. F3 in Appendix F).

310 The new Os data from Cau (see fig. 3) show a low concentration of Os
 311 with a slight trend towards more radiogenic values (> 1) towards the start of the
 312 negative CIE (40-45 m). This is followed by increasing Os concentration during
 313 the CIE, its isotopic composition shifting to less radiogenic values (< 0.4). A
 314 brief excursion back to low concentrations of very radiogenic Os (> 1.2) half
 315 way through the negative CIE onset (~ 55 m) is based on two data points. All
 316 data can be found in Appendix E.

317 **4. Discussion**

318 Our inverse modelling suggests that the addition of ^{13}C -depleted carbon dur-
 319 ing the start of the negative CIE (Phase A in fig. 4), followed by sustained input
 320 of carbon with a largely volcanic isotopic signature (Phase B, typically between
 321 -5 and -8 ‰ away from subduction zones (Javoy et al., 1986)), reconciles the
 322 measured $\delta^{13}\text{C}_{carb}$ and reconstructed $p\text{CO}_2$ at Cau (Naafs et al., 2016). Our

323 method results in required ‘net’ carbon fluxes and their isotopic compositions.
 324 While we cannot exclude mixes of sources (and sinks) that sum to the right
 325 ‘net’ values, this provides information about the dominant carbon source. The
 326 requirement for initial carbon emissions more ^{13}C -depleted than volcanic CO_2
 327 across our simulations indicates that contribution from organic carbon sources
 328 (typically between -10 and -30 ‰ (e.g. Meyers, 1994)) and methane, the only
 329 surficial carbon with a $\delta^{13}\text{C} < -40$ ‰, was necessary to drive the CIE at the
 330 OAE 1a onset (see fig. 2b,d and Appendix). Predominant methane emissions,
 331 however, are only required in scenarios with minimal $p\text{CO}_2$ rise during the CIE
 332 onset. All scenarios require the most ^{13}C -depleted carbon input between 48 m
 333 and 52 m. The isotopic composition of the carbon input predicted by cGENIE
 334 between 52 m and 58 is consistently less depleted (around or above -10 ‰ for
 335 most simulations) almost regardless of uncertainty in reconstructed $p\text{CO}_2$ or
 336 duration. This is consistent only with an appreciable contribution from a vol-
 337 canic source. The shift in source from sedimentary organic carbon to volcanism
 338 occurs relatively rapidly, within 4 m at Cau or 25 kyr assuming a negative CIE
 339 onset duration of 100 kyr and a constant sedimentation rate. Importantly, this
 340 difference in isotopic composition between strata below and above 52 m is a
 341 robust feature in all simulations and suggests that Earth’s system transitioned
 342 from predominant input from an isotopically light carbon source to a heavier
 343 one. Scenarios with low $p\text{CO}_2$ increase require another pulse of biogenic CO_2
 344 to reach the lowest $\delta^{13}\text{C}$ values at the end of our simulations, while the isotopic
 345 signature of carbon inputs in scenarios with higher emission rates remains close

346 to mantle values.

347 A shift to a more mantle-like source is supported by published Os isotope
348 data which have been used to infer changes in volcanic activity across OAEs,
349 given that the main source of unradiogenic Os is mantle material (Turgeon &
350 Creaser, 2008; Bottini et al., 2012; Du Vivier et al., 2014). Published OAE 1a Os
351 isotope records from pelagic sections show a shift towards unradiogenic (mantle-
352 like) values during the negative CIE at the onset of OAE 1a (Bottini et al., 2012),
353 suggesting a strengthened Os flux from the mantle. While a direct comparison
354 between Os records from Cau and other sites is hampered by uncertainties in
355 age models and missing stratigraphic ties, records from all sites show similar
356 features. The consistent shift to very unradiogenic Os-isotope values in the Cau
357 record (fig. 4) is similar to that recorded in other sections and adds confidence
358 to the assumption that strengthened volcanism was the primary control on Os
359 isotope changes recorded across the negative CIE at Cau, even more so given the
360 small amount of preserved organic matter preserved and its platform setting.
361 Similar to other Tethyan sections, the Os record at Cau shows a shift back to
362 radiogenic values before stagnating at unradiogenic values (in phase B in fig. 4,
363 Jenkyns (2018)). Since this excursion is not evident in records from all OAE
364 1a sections, it might represent a local or regional change with little implications
365 for the reconstructed volcanic strength. In that case the shifts from less to
366 more mantle-like compositions of Os and carbon coincide at Cau (fig. 4). If
367 the radiogenic excursion at ~ 55 m in the Cau section reflects a global change
368 of Os fluxes, the resolution of the $p\text{CO}_2$ reconstruction is either too coarse to

369 evidence a short-term decline in volcanic carbon emissions, or the relationship
370 between carbon and Os isotopic changes during the onset of LIP emplacement
371 is more complex. At this moment, we cannot test this relationship at other
372 sites because combined records of Os isotope and inferred $p\text{CO}_2$ changes are
373 not available at the required resolution.

374 Emissions of carbon from an organic matter reservoir are needed to explain
375 carbon isotopic changes at Cau regardless of the $p\text{CO}_2$ scenario or assumed du-
376 ration of CIE onset. However the exact mechanism of its release at the onset of
377 OAE 1a is not clear. It is unlikely that depleted carbon was emitted due to feed-
378 back mechanisms in response to a warming climate (e.g. destabilized methane
379 hydrates), given the small changes in atmospheric $p\text{CO}_2$ at that time. There is,
380 however, evidence in support of geologically-triggered emissions of ^{13}C -depleted
381 organic carbon during the onset of OAE 1a. Polteau et al. (2016) showed that
382 magma intrusions into overlying sediments during the formation of the Barents
383 Sea Sill Complex in the early Aptian could have destabilized a considerable mass
384 of organic carbon and led to thermogenic methane emissions. OAE 1a happened
385 at a time of high magmatic activity, including the emplacement phases of the
386 Ontong-Java Plateau LIP (e.g. Larson & Erba, 1999). We therefore suggest
387 that at the start of the negative CIE magmatic activity increased under thin
388 crust, intruding into organic-rich marine sediments and causing small releases of
389 ^{13}C -depleted thermogenic gases. This initial phase of increased mantle activity
390 was then followed by a more eruptive phase of LIP emplacement, when large-
391 scale submarine volcanism dominated exogenic carbon emissions and delivered

392 large amounts of new mantle material to the ocean floor. This increased the
 393 flux of unradiogenic Os into the ocean through hydrothermal vents as well as
 394 weathering of fresh basalt and released vast amounts of mantle-sourced carbon
 395 to the atmosphere. Thus, the initial $\delta^{13}\text{C}$ decrease and the excursions in Os iso-
 396 topes and $\Delta^{13}\text{C}$ are consistent with a scenario in which the recorded CIE and
 397 $p\text{CO}_2$ change occurred independently: The first through release of sedimentary
 398 organic carbon, and the latter through volcanic CO_2 emissions.

399 Our results based on records of atmospheric $p\text{CO}_2$ and $\delta^{13}\text{C}$ are consistent
 400 with published model interpretations of Os isotope profiles, which also find
 401 that volcanism was the primary carbon source during OAE 1a (Bauer et al.,
 402 2017). The mass of emitted carbon in our results is however different from that
 403 reconstructed by Bauer et al. (2017) using Os isotopes. The biomarker-based
 404 estimate suggests an increase in $p\text{CO}_2$ of 200-1700 ppm (Naafs et al., 2016),
 405 whereas the model interpretation of $^{187}\text{Os}/^{188}\text{Os}$ implies that $p\text{CO}_2$ rose by
 406 about 3,000 ppm (Bauer et al., 2017). We tested the implications for carbon
 407 sources assuming a continuous CO_2 concentration increase of 3000 ppm, which
 408 resulted in increased carbon emissions ($0.32 \text{ Pg C yr}^{-1}$ assuming a 100 kyr
 409 duration, see fig. D4 in the appendix) compared to our scenarios, with isotopic
 410 compositions between -20 and -3 ‰. This is still consistent with a predominantly
 411 volcanic source, but reduced the need for more ^{13}C -depleted organic carbon
 412 release. Temperature proxy records across OAE 1a (Mutterlose et al., 2014;
 413 Naafs & Pancost, 2016) are consistent with regional temperature changes of 1-5
 414 °C produced by scenarios based on the Naafs et al. (2016) $p\text{CO}_2$ reconstruction.

415 The higher (Os based) $p\text{CO}_2$ changes result in a temperature rise of 7 °C globally
416 in cGENIE, equivalent to 5 – 6 °C in the Tethys which is at the upper end of
417 reconstructed temperature change.

418 Organic carbon burial is not simulated by our model, meaning that we have
419 to assume that organic carbon burial did not strengthen significantly during the
420 negative CIE onset. Although carbon contents at Cau and at other locations
421 only increase during the recovery of the negative CIE and start of the positive
422 CIE (generally referred to as segments C4-C6 Menegatti et al., 1998; Quijano
423 et al., 2012; Erba et al., 2015), it is unknown to what degree the marine carbon
424 and Os cycles were influenced by organic matter burial locally and/or globally.
425 Widespread organic carbon burial would shorten the residence time of Os and
426 carbon in the ocean and create a sink for ^{12}C , increasing carbon emission rates
427 needed to produce the observed environmental changes. The results from our
428 experiments should thus be regarded as a low-end estimate of the mass of emit-
429 ted carbon. However, our experiments indicate that the transition from more
430 ^{13}C depleted organic carbon input (potentially from sill intrusions) to mantle-
431 sourced carbon (volcanism) is robust against changes in emission rate and total
432 mass of emitted carbon and hence should be detectable despite changes in the
433 amount of organic matter burial.

434 In terms of timing, high-resolution temperature records (based on palynology
435 and $\delta^{18}\text{O}$) at the expanded pelagic section of Pusiano and the shelf section
436 at La Bédoule (Keller et al., 2011; Lorenzen et al., 2013) indicate a time lag
437 between the start of the negative CIE and the main period of warming. This

would be consistent with our reconstructed emissions scenarios. At pelagic sections lower sediment accumulation rates and coarser sampling resolutions (e.g. Cismon, Roter Sattel, Pacific DSDP site 463 and Atlantic DSDP site 398), likely prevented the identification of such time lag between temperature proxies and negative CIE (Menegatti et al., 1998; Ando et al., 2008; Naafs & Pancost, 2016).

Major changes in the marine nannofossil community, including dwarfism, and a decline in CaCO_3 burial rates, have been observed during the negative CIE and interpreted as an indicator for a decline in calcite surface ocean saturation state due to large carbon emissions (Weissert & Erba, 2004; Erba et al., 2010). The widespread occurrence of surface ocean acidification during OAE 1a as driver of biological turn-over is contested (Gibbs et al., 2011; Naafs et al., 2016). Our simulations show that only scenarios with a large carbon source or short event duration result in an appreciable Ω decline ($\Delta\Omega > 0.5$), globally and locally. A decrease in saturation state could have imposed significant stress onto calcifiers (Weissert & Erba, 2004). At Cau, the $p\text{CO}_2$ changes and the decline in Ω (around 54 m) began well after the onset of the nannofossil decline, which starts at 43 m. In our longer simulations (≥ 100 kyr) increased weathering and continental runoff eventually counteract the CO_2 dissolution effect, which leads to a recovered or even increased calcite saturation state at the end of these experiments, despite ongoing carbon emissions. Further quantitative comparison of the impact of carbon emissions onto the surface ocean carbonate chemistry in our simulations is hampered by remaining uncertainties. For ex-

ample, the carbonate system of the pre-OAE 1a Aptian surface ocean is poorly constrained. Particularly the mass of emitted carbon needed to cause appreciable Ω changes and the position of the carbonate compensation depth depend largely on these initial conditions. The slow carbon emission rates predicted by our model are also a function of the duration of the negative CIE onset. Unless the onset took 20 kyr (Malinverno et al., 2010, the smallest current estimate) or less, it is unlikely that carbon emissions could have outpaced the weathering feedbacks that stabilize the surface ocean saturation state (Hönisch et al., 2012). As such, estimated onset durations and the temporal decoupling between changes in calcite saturation state and nannoconid crisis make it unlikely that this major perturbation of the marine nanno-calcifier community was a direct result of carbon emissions driving the negative CIE.

5. Conclusion

We used transient model simulations based on combined $p\text{CO}_2$ and $\delta^{13}\text{C}$ records to identify dominant carbon sources and quantify associated emission rates. The simulations show that carbon emission rates of 0.043-1.46 Pg C yr^{-1} reconcile the negative CIE and $p\text{CO}_2$ estimates, with the exact rate depending on the assumed duration of OAE onset. Assuming a baseline $p\text{CO}_2$ of 850 ppm this is consistent with estimates of moderate temperature change from diverse proxy data. Our results suggest that an initial input of predominantly ^{13}C -depleted carbon was responsible for the negative CIE associated with OAE 1a, but had little effect on atmospheric $p\text{CO}_2$. This carbon could have

483 originated from sill intrusions into marine organic rich sediments, potentially
484 releasing thermogenic and/or biogenic methane. Following this initial phase,
485 volcanic (less ^{13}C -depleted) carbon emissions sustained the stagnant part of the
486 negative CIE and fuelled most of the recorded atmospheric $p\text{CO}_2$ increase. Our
487 results indicate that organic carbon emissions in form of methane and/or CO_2 ,
488 despite shaping the $\delta^{13}\text{C}$ curve, did not increase the atmospheric carbon reser-
489 voir appreciably. Importantly, this demonstrates that the scale and nature of
490 the Earth system perturbation at the onset of OAE 1a cannot be determined
491 based on the existence of a negative CIE or its size alone. This may also be
492 the case for other negative CIEs in the geological record. Our results further
493 imply the possibility of a time lag between the carbon isotopic excursion and
494 the major phase of carbon emissions, but highly resolved records from other
495 sections are necessary to corroborate this finding. Uncertainties in the amount
496 of atmospheric $p\text{CO}_2$ change and duration of the OAE onset create propor-
497 tionally large uncertainties on carbon emission rates and their initial isotopic
498 composition. Increased accuracy in duration and $p\text{CO}_2$ change estimates are
499 needed to narrow down our estimates of carbon flux magnitudes and origins.
500 However, the shift from more to less ^{13}C -depleted carbon emissions is robust
501 against these uncertainties, as are the pure volcanic-like carbon fluxes towards
502 the peak of the negative CIE. We conclude that mantle activity increased in the
503 early Aptian, heating organic-rich marine sediments and releasing thermogenic
504 methane before sustained mantle eruptions led to OAE formation.

505 **Acknowledgements**

506 We would like to thank Stephen Hesselbo and Sandra Kirtland Turner for
507 helpful discussions of, and comments on, the study design. We also want to
508 acknowledge the constructive comments by two anonymous reviewers, which
509 helped us to improve the manuscript.

510 Furthermore, we would like to thank our funding bodies: M.A. was sup-
511 ported by the NERC GW4+ DTP and the Natural Environment Research Coun-
512 cil [NE/L002434/1]. S.E.G. was supported by NERC grants NE/L011050/1
513 and NE/P01903X/1 while working on this manuscript. FMM was supported
514 by a NERC research fellowship (NE/J019062/1) and a NERC standard grant
515 (NE/N011112/1). B.D.A.N. was funded through a Royal Society Tata Univer-
516 sity Research Fellowship. W.P. was supported by ERC Grant Agreement no.
517 340923. J.M.C. has received funding from the Spanish Ministry of Science and
518 Technology (project CGL2014-55274-P) and Reseach Group RNM-200 (Junta
519 de Andalucía).

520 **Code Availability**

521 *muffin overview*

522 The code for the cGENIE.muffin model is hosted on GitHub. The current
523 version can be obtained by cloning:

524 <https://github.com/derpycode/cgenie.muffin>

525 A manual, detailing code installation, basic model configuration, plus an exten-
526 sive series of tutorials covering various aspects of muffin capability, experimental

527 design, and results output and processing, is provided. A PDF of the manual
528 can be downloaded here:

529 <http://www.seao2.info/cgenie/docs/muffin.pdf>

530 The latex source and most up-to-date built PDF file can be obtained by cloning:

531 <https://github.com/derpycode/muffindoc>

532 *Instructions summary*

533 The muffin manual contains instructions for obtaining, installing, and testing
534 the code, plus how to run experiments. Specifically:

535 **Section 1.1** – provides a basic over-view of the software environment required
536 for installing and running muffin.

537 **Section 1.2.2** – provides a basic over-view of cloning and testing the code.

538 **Section 15.4** – provides a detailed guide to cloning the code and configuring a
539 Ubuntu (18.04) software environment including netCDF library installa-
540 tion, plus running a basic test.

541 **Section 15.6** – provides a detailed guide to cloning the code and configuring a
542 macOS software environment including netCDF library installation, plus
543 running a basic test.

544 **Section 1.3** – provides a basic guide to running experiments (also see 1.6 and
545 1.7).

546 **Section 1.4** – provides a basic introduction to model output (much more detail
547 is given in Section 12).

548 *Model experiments*

549 Configuration files for the specific experiments presented in the paper can be
550 found in the directory:

551 `cgenie.muffin\genie-userconfigs\MS\adloffetal.2019`

552 Details of the different experiments, plus the command line needed to run each
553 one, are given in `readme.txt`.

554 **References**

555 Aguado, R., Castro, J. M., Company, M., & De Gea, G. A. (1999). Aptian bio-
556 events—an integrated biostratigraphic analysis of the Almadich Formation,
557 Inner Prebetic Domain, SE Spain. *Cretaceous Research*, *20*, 663–683.

558 Ando, A., Kaiho, K., Kawahata, H., & Kakegawa, T. (2008). Timing and mag-
559 nitude of early Aptian extreme warming: unraveling primary $\delta^{18}\text{O}$ variation
560 in indurated pelagic carbonates at Deep Sea Drilling Project Site 463, cen-
561 tral Pacific Ocean. *Palaeogeography, Palaeoclimatology, Palaeoecology*, *260*,
562 463–476.

563 Bauer, K. W., Zeebe, R. E., & Wortmann, U. G. (2017). Quantifying the
564 volcanic emissions which triggered Oceanic Anoxic Event 1a and their effect
565 on ocean acidification. *Sedimentology*, *64*, 204–214.

566 Beerling, D. J., Lomas, M., & Gröcke, D. R. (2002). On the nature of
567 methane gas-hydrate dissociation during the Toarcian and Aptian oceanic
568 anoxic events. *American Journal of Science*, *302*, 28–49.

569 Birck, J. L., Barman, M. R., & Capmas, F. (1997). Re-Os isotopic measurements
570 at the femtomole level in natural samples. *Geostandards newsletter*, *21*, 19–
571 27.

572 Bottini, C., Cohen, A. S., Erba, E., Jenkyns, H. C., & Coe, A. L. (2012).
573 Osmium-isotope evidence for volcanism, weathering, and ocean mixing during
574 the early Aptian OAE 1a. *Geology*, *40*, 583–586.

575 van Breugel, Y., Schouten, S., Tsikos, H., Erba, E., Price, G. D., & Sin-
576 ninghe Damsté, J. S. (2007). Synchronous negative carbon isotope shifts
577 in marine and terrestrial biomarkers at the onset of the early Aptian oceanic
578 anoxic event 1a: Evidence for the release of ^{13}C -depleted carbon into the
579 atmosphere. *Paleoceanography*, *22*, PA1210.

580 Castro, J., De Gea, G., Ruiz-Ortiz, P., & Nieto, L. (2008). Development of car-
581 bonate platforms on an extensional (rifted) margin: the Valanginian–Albian
582 record of the Prebetic of Alicante (SE Spain). *Cretaceous Research*, *29*, 848–
583 860.

584 Colbourn, G., Ridgwell, A., & Lenton, T. (2013). The rock geochemical model
585 (rokgem) v0. 9. *Geoscientific Model Development*, *6*, 1543–1573.

586 Craig, H. (1953). The geochemistry of the stable carbon isotopes. *Geochimica*
587 *et Cosmochimica Acta*, *3*, 53–92.

588 Cui, Y., Kump, L. R., Ridgwell, A. J., Charles, A. J., Junium, C. K., Diefendorf,
589 A. F., Freeman, K. H., Urban, N. M., & Harding, I. C. (2011). Slow release

590 of fossil carbon during the Palaeocene–Eocene Thermal Maximum. *Nature*
591 *Geoscience*, *4*, 481.

592 Donnadieu, Y., Pierrehumbert, R., Jacob, R., & Fluteau, F. (2006). Modelling
593 the primary control of paleogeography on Cretaceous climate. *Earth and*
594 *Planetary Science Letters*, *248*, 426–437.

595 Du Vivier, A. D., Selby, D., Sageman, B. B., Jarvis, I., Gröcke, D. R., & Voigt,
596 S. (2014). Marine $^{187}\text{Os}/^{188}\text{Os}$ isotope stratigraphy reveals the interaction of
597 volcanism and ocean circulation during Oceanic Anoxic Event 2. *Earth and*
598 *Planetary Science Letters*, *389*, 23–33.

599 Edwards, N. R., & Marsh, R. (2005). Uncertainties due to transport-parameter
600 sensitivity in an efficient 3-D ocean-climate model. *Climate Dynamics*, *24*,
601 415–433.

602 Erba, E., Bottini, C., Weissert, H. J., & Keller, C. E. (2010). Calcareous
603 nannoplankton response to surface-water acidification around Oceanic Anoxic
604 Event 1a. *Science*, *329*, 428–432.

605 Erba, E., Duncan, R. A., Bottini, C., Tiraboschi, D., Weissert, H., Jenkyns,
606 H. C., & Malinverno, A. (2015). Environmental consequences of Ontong
607 Java Plateau and Kerguelen Plateau volcanism. *The origin, evolution, and*
608 *environmental impact of oceanic large igneous provinces. Geological Society*
609 *of America Special Paper*, *511*, 271–303.

610 Gibbs, S. J., Robinson, S. A., Bown, P. R., Jones, T. D., & Henderiks, J.

611 (2011). Comment on “Calcareous nannoplankton response to surface-water
 612 acidification around Oceanic Anoxic Event 1a”. *Science*, *332*, 175–175.

613 Gutjahr, M., Ridgwell, A., Sexton, P. F., Anagnostou, E., Pearson, P. N., Pälike,
 614 H., Norris, R. D., Thomas, E., & Foster, G. L. (2017). Very large release of
 615 mostly volcanic carbon during the Palaeocene–Eocene Thermal Maximum.
 616 *Nature*, *548*, 573.

617 Hönisch, B., Ridgwell, A., Schmidt, D. N., Thomas, E., Gibbs, S. J., Sluijs, A.,
 618 Zeebe, R., Kump, L., Martindale, R. C., Greene, S. E. et al. (2012). The
 619 geological record of ocean acidification. *Science*, *335*, 1058–1063.

620 Hu, X., Zhao, K., Yilmaz, I. O., & Li, Y. (2012). Stratigraphic transition
 621 and palaeoenvironmental changes from the Aptian oceanic anoxic event 1a
 622 (OAE1a) to the oceanic red bed 1 (ORB1) in the Yenicesihlar section, central
 623 Turkey. *Cretaceous Research*, *38*, 40–51.

624 Javoy, M., Pineau, F., & Delorme, H. (1986). Carbon and nitrogen isotopes in
 625 the mantle. *Chemical Geology*, *57*, 41–62.

626 Jenkyns, H. C. (2010). Geochemistry of oceanic anoxic events. *Geochemistry*,
 627 *Geophysics, Geosystems*, *11*, Q03004.

628 Jenkyns, H. C. (2018). Transient cooling episodes during Cretaceous Oceanic
 629 Anoxic Events with special reference to OAE 1a (Early Aptian). *Philosophical*
 630 *Transactions of the Royal Society A: Mathematical, Physical and Engineering*
 631 *Sciences*, *376*, 20170073.

632 John, E. H., Wilson, J. D., Pearson, P. N., & Ridgwell, A. (2014). Temperature-
633 dependent remineralization and carbon cycling in the warm Eocene oceans.
634 *Palaeogeography, palaeoclimatology, palaeoecology*, 413, 158–166.

635 Josso, P., Parkinson, I., Horstwood, M., Lusty, P., Chenery, S., & Murton, B.
636 (2019). Complementarity of Co-chronometry, LA-ICP-MS and Os isotopes
637 for the development of composite age model for deep-ocean ferromanganese
638 crust. *Chemical Geology*, 513, 108–119.

639 Keller, C. E., Hochuli, P. A., Weissert, H., Bernasconi, S. M., Giorgioni, M.,
640 & Garcia, T. I. (2011). A volcanically induced climate warming and floral
641 change preceded the onset of OAE1a (Early Cretaceous). *Palaeogeography,*
642 *Palaeoclimatology, Palaeoecology*, 305, 43–49.

643 Kirtland-Turner, S., & Ridgwell, A. (2016). Development of a novel empirical
644 framework for interpreting geological carbon isotope excursions, with implica-
645 tions for the rate of carbon injection across the PETM. *Earth and Planetary*
646 *Science Letters*, 435, 1–13.

647 Larson, R. L., & Erba, E. (1999). Onset of the Mid-Cretaceous greenhouse in
648 the Barremian-Aptian: Igneous events and the biological, sedimentary, and
649 geochemical responses. *Paleoceanography*, 14, 663–678.

650 Li, Y.-X., Bralower, T. J., Montañez, I. P., Osleger, D. A., Arthur, M. A., Bice,
651 D. M., Herbert, T. D., Erba, E., & Silva, I. P. (2008). Toward an orbital
652 chronology for the early Aptian oceanic anoxic event (OAE1a, ~ 120 Ma).
653 *Earth and Planetary Science Letters*, 271, 88–100.

654 Lorenzen, J., Kuhnt, W., Holbourn, A., Flögel, S., Moullade, M., & Tronchetti,
 655 G. (2013). A new sediment core from the Bedoulian (Lower Aptian) stratotype
 656 at Roquefort-La Bédoule, SE France. *Cretaceous Research*, 39, 6–16.

657 Malinverno, A., Erba, E., & Herbert, T. (2010). Orbital tuning as an inverse
 658 problem: Chronology of the early Aptian oceanic anoxic event 1a (Selli Level)
 659 in the Cismon APTICORE. *Paleoceanography*, 25, PA2203.

660 Méhay, S., Keller, C. E., Bernasconi, S. M., Weissert, H., Erba, E., Bottini,
 661 C., & Hochuli, P. A. (2009). A volcanic CO₂ pulse triggered the Cretaceous
 662 Oceanic Anoxic Event 1a and a biocalcification crisis. *Geology*, 37, 819–822.

663 Menegatti, A. P., Weissert, H., Brown, R. S., Tyson, R. V., Farrimond, P.,
 664 Strasser, A., & Caron, M. (1998). High-resolution $\delta^{13}\text{C}$ stratigraphy through
 665 the early Aptian “Livello Selli” of the Alpine Tethys. *Paleoceanography*, 13,
 666 530–545.

667 Meyers, P. A. (1994). Preservation of elemental and isotopic source identification
 668 of sedimentary organic matter. *Chemical Geology*, 114, 289–302.

669 Miller, C. A., Peucker-Ehrenbrink, B., & Ball, L. (2009). Precise determination
 670 of rhenium isotope composition by multi-collector inductively-coupled plasma
 671 mass spectrometry. *Journal of Analytical Atomic Spectrometry*, 24, 1069–
 672 1078.

673 Monteiro, F. M., Pancost, R. D., Ridgwell, A., & Donnadieu, Y. (2012). Nu-
 674 trients as the dominant control on the spread of anoxia and euxinia across

675 the Cenomanian-Turonian oceanic anoxic event (OAE2): Model-data com-
 676 parison. *Paleoceanography*, *27*, PA4209.

677 Mutterlose, J., Bottini, C., Schouten, S., & Sinninghe Damsté, J. S. (2014).
 678 High sea-surface temperatures during the early Aptian Oceanic Anoxic Event
 679 1a in the Boreal Realm. *Geology*, *42*, 439–442.

680 Naafs, B., Castro, J., De Gea, G., Quijano, M., Schmidt, D., & Pancost, R.
 681 (2016). Gradual and sustained carbon dioxide release during Aptian Oceanic
 682 Anoxic Event 1a. *Nature Geoscience*, *9*, 135–139.

683 Naafs, B., & Pancost, R. (2016). Sea-surface temperature evolution across Ap-
 684 tian Oceanic Anoxic Event 1a. *Geology*, *44*, 959–962.

685 Olierook, H. K., Jourdan, F., & Merle, R. E. (2019). Age of the Barremian–
 686 Aptian boundary and onset of the Cretaceous Normal Superchron. *Earth-*
 687 *Science Reviews*, (p. 102906).

688 Polteau, S., Hendriks, B. W., Planke, S., Ganerød, M., Corfu, F., Faleide, J. I.,
 689 Midtkandal, I., Svensen, H. S., & Myklebust, R. (2016). The Early Creta-
 690 ceous Barents Sea sill complex: distribution, $^{40}\text{Ar}/^{39}\text{Ar}$ geochronology, and
 691 implications for carbon gas formation. *Palaeogeography, Palaeoclimatology,*
 692 *Palaeoecology*, *441*, 83–95.

693 Popp, B. N., Laws, E. A., Bidigare, R. R., Dore, J. E., Hanson, K. L., &
 694 Wakeham, S. G. (1998). Effect of phytoplankton cell geometry on carbon
 695 isotopic fractionation. *Geochimica et cosmochimica acta*, *62*, 69–77.

696 Quijano, M. L., Castro, J. M., Pancost, R. D., de Gea, G. A., Najarro, M.,
 697 Aguado, R., Rosales, I., & Martín-Chivelet, J. (2012). Organic geochemistry,
 698 stable isotopes, and facies analysis of the Early Aptian OAE—New records
 699 from Spain (Western Tethys). *Palaeogeography, Palaeoclimatology, Palaeo-*
 700 *cology*, *365*, 276–293.

701 Ridgwell, A., & Hargreaves, J. (2007). Regulation of atmospheric CO₂ by deep-
 702 sea sediments in an Earth system model. *Global Biogeochemical Cycles*, *21*,
 703 GB2008.

704 Ridgwell, A., Hargreaves, J., Edwards, N. R., Annan, J., Lenton, T. M., Marsh,
 705 R., Yool, A., & Watson, A. (2007). Marine geochemical data assimilation in
 706 an efficient Earth System Model of global biogeochemical cycling. *Biogeo-*
 707 *sciences*, *4*, 87–104.

708 Ridgwell, A., & Schmidt, D. N. (2010). Past constraints on the vulnerability
 709 of marine calcifiers to massive carbon dioxide release. *Nature Geoscience*, *3*,
 710 196.

711 Ridgwell, A., & Zeebe, R. E. (2005). The role of the global carbonate cycle
 712 in the regulation and evolution of the earth system. *Earth and Planetary*
 713 *Science Letters*, *234*, 299–315.

714 Schlanger, S. O., & Jenkyns, H. (1976). Cretaceous oceanic anoxic events:
 715 causes and consequences. *Netherlands Journal of Geosciences/Geologie en*
 716 *Mijnbouw*, *55*, 179–184.

- 717 Shirey, S. B., & Walker, R. J. (1995). Carius tube digestion for low-blank
718 rhenium-osmium analysis. *Analytical Chemistry*, *67*, 2136–2141.
- 719 Tejada, M. L. G., Suzuki, K., Kuroda, J., Coccioni, R., Mahoney, J. J., Ohk-
720 ouchi, N., Sakamoto, T., & Tatsumi, Y. (2009). Ontong Java Plateau eruption
721 as a trigger for the early Aptian oceanic anoxic event. *Geology*, *37*, 855–858.
- 722 Turgeon, S. C., & Creaser, R. A. (2008). Cretaceous oceanic anoxic event 2
723 triggered by a massive magmatic episode. *Nature*, *454*, 323.
- 724 Turner, S. K., & Ridgwell, A. (2013). Recovering the true size of an Eocene
725 hyperthermal from the marine sedimentary record. *Paleoceanography*, *28*,
726 700–712.
- 727 Wang, Y., Huang, C., Sun, B., Quan, C., Wu, J., & Lin, Z. (2014). Paleo-
728 CO₂ variation trends and the Cretaceous greenhouse climate. *Earth-Science*
729 *Reviews*, *129*, 136–147.
- 730 Weissert, H. (1989). C-isotope stratigraphy, a monitor of paleoenvironmental
731 change: a case study from the Early Cretaceous. *Surveys in Geophysics*, *10*,
732 1–61.
- 733 Weissert, H., & Erba, E. (2004). Volcanism, CO₂ and palaeoclimate: a Late
734 Jurassic–Early Cretaceous carbon and oxygen isotope record. *Journal of the*
735 *Geological Society*, *161*, 695–702.
- 736 Wissler, L., Funk, H., & Weissert, H. (2003). Response of Early Cretaceous

737 carbonate platforms to changes in atmospheric carbon dioxide levels. *Palaeo-*
 738 *geography, Palaeoclimatology, Palaeoecology*, 200, 187–205.

739 Figures

a) Reconstructed atmospheric carbon b) Model forcing for stage C3
 across OAE 1a

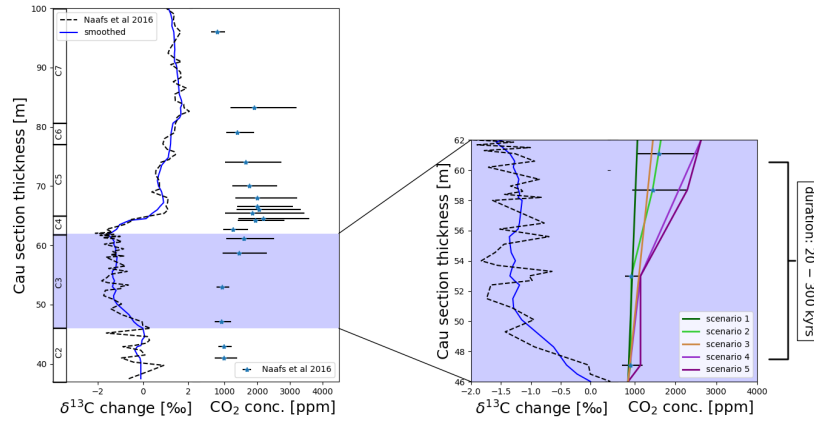
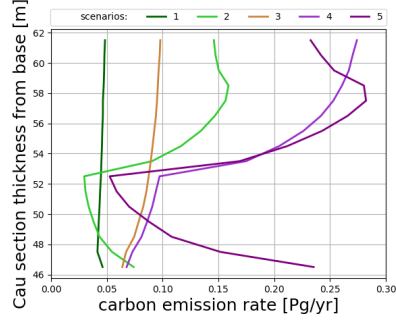
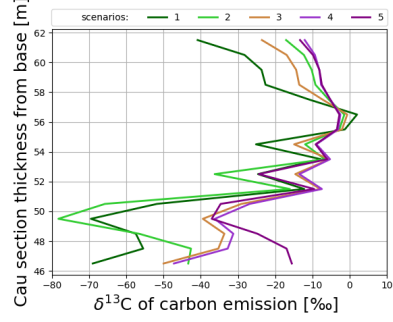


Figure 1: Reconstructed properties of the surficial carbon reservoir during OAE 1a (segments after Naafs et al. (2016)) and $p\text{CO}_2$ forcings used in this study. a) Reconstruction of bulk carbonate $\delta^{13}\text{C}$ variation and $p\text{CO}_2$ across OAE 1a based on proxy data from Cau (Naafs et al. 2016a): b) Zoom into the onset of the negative CIE, showing $\delta^{13}\text{C}$ changes and the 5 $p\text{CO}_2$ scenarios we tested in cGENIE. $\delta^{13}\text{C}$ values are given as offsets from the highest value in the smoothed $\delta^{13}\text{C}_{carb}$ data series prior to the start of OAE 1a.

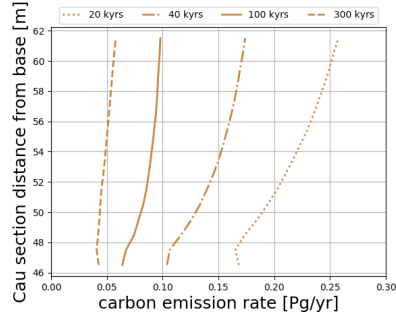
a) carbon mass fluxes across stage C3



b) $\delta^{13}\text{C}$ of carbon fluxes



c) carbon masses with different C3 duration estimates



d) $\delta^{13}\text{C}$ with different duration estimates

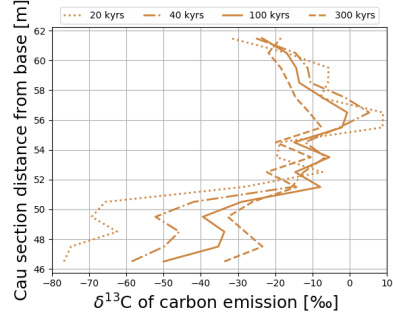


Figure 2: Carbon fluxes and their isotopic signatures across the onset of the negative CIE as calculated by cGENIE. (a) and (b) show differences due to different $p\text{CO}_2$ change scenarios (see fig. 1), all assuming a CIE onset duration of 100 kyr. (c) and (d) show the influence of a different CIE onset duration (20-300 kyr) exemplarily for scenario 3. The results are averaged over 1m depth equivalent.

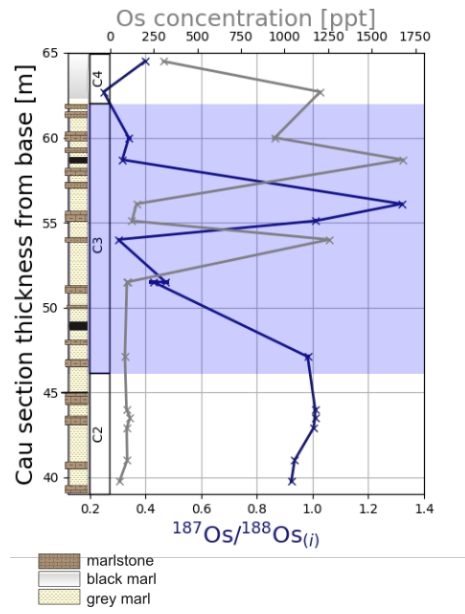


Figure 3: Os concentration and $^{187}\text{Os}/^{188}\text{Os}_{(i)}$ between meters 39 and 65 of the Cau section. The onset of the negative CIE is marked by blue shading. Uncertainties on data are smaller than the symbols.

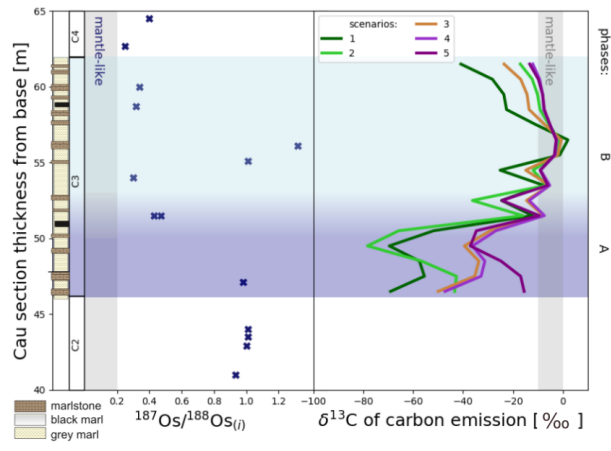


Figure 4: Osmium isotopic changes (left) and reconstructed $\delta^{13}\text{C}$ signature of emissions based on carbon isotopes (right) at Cau. The two shaded sections show phases of least (A) and most prominent (B) volcanic activity.